Microstructure and morphology of Si crystals grown in pure Si and Al–Si melts

OPEN ACCESS
IOP Publishing
Journal of Physics: Condensed Matter
J. Phys.: Condens. Matter **34** (2022) 094002 (7pp)
https://doi.org/10.1088/1361-648X/ac3792

Microstructure and morphology of Si crystals grown in pure Si and Al–Si melts

L V Toropova[1,2,*], D V Alexandrov[1], M Rettenmayr[2] and D Liu[2]

[1] Laboratory of Multi-Scale Mathematical Modeling, Department of Theoretical and Mathematical Physics, Ural Federal University, Ekaterinburg, 620000, Russia
[2] Otto-Schott-Institut für Materialforschung, Friedrich-Schiller-Universität-Jena, 07743 Jena, Germany

E-mail: l.v.toropova@urfu.ru

Received 7 October 2021
Accepted for publication 8 November 2021
Published 10 January 2022

Abstract

Microstructure of Al-40 wt%Si samples solidified in electromagnetic levitation furnace is studied at high melt undercooling. Primary Si with feathery and dendritic structures is observed. As this takes place, single Si crystals either contain secondary dendrite arms or represent faceted structures. Our experiments show that at a certain undercooling, there exists the microstructural transition zone of faceted to non-faceted growth. Also, we analyze the shape of dendritic crystals solidifying from liquid Si as well as from hypereutectic Al–Si melts at high growth undercoolings. The shapes of dendrite tips grown at undercoolings >100 K along the surface of levitated Al-40 wt%Si droplets are compared with pure Si dendrite tips from the literature. The dendrite tips are digitized and superimposed with theoretical shape function recently derived by stitching the Ivantsov and Brener solutions. We show that experimental and theoretical dendrite tips are in good agreement for Si and Al–Si samples.

Keywords: dendrite, phase transformation, silicon, interface shape, dendrite tip

(Some figures may appear in colour only in the online journal)

1. Introduction

It is well known that Si is a semiconductor material that generally solidifies in a faceted manner. This is in accordance with the theory that a dimensionless melting entropy ($\Delta S_f/R$) above ~2 leads to faceting. An estimation that is a little more sophisticated does not only consider the bulk melting entropy, but the situation at the growing interface, and the 'Jackson factor' α [1] contains, additionally to the dimensionless melting entropy, the number of bondings at the interface and the coordination number, resulting in $\alpha = 3.6$. This also predicts faceted solidification, but is close to the limit where also non-faceted growth with parabolic dendrite tips can occur.

Faceted growth has been observed in numerous cases at low undercoolings. However, it has been shown that at high undercoolings $\Delta T > 240$ K, Si dendrites solidify with a parabolic, non-faceted interface, and transitional regimes between faceted and non-faceted growth have been observed, without a precise specification of these transitions [2, 3]. The growth velocity vs undercooling relationship for pure Si dendrites has been investigated in electromagnetic levitation (EML) experiments [4–6]. It has been found that in the undercooling regime above $\Delta T \approx 100$ K, growing dendrite tips may appear both as faceted or parabolic. The growth velocity vs undercooling relationship can semi-quantitatively be reproduced by the LKT model [7], even though this model assumes isotropic interfacial energy, which for Si is not an appropriate assumption.

Evidently, Si dendrites will grow from pure Si melts, but they will also grow from binary alloy melts, if Si is the primarily solidifying phase and does not dissolve notable amounts of the secondary alloy element, such as in Al–Si alloys [8]. The difference in the growth kinetics between pure Si

* Author to whom any correspondence should be addressed.

1361-648X/22/094002+7$33.00

dendrites growing from a pure or alloy melt, respectively, is to be expected on the one hand in the interface attachment kinetics (as less Si atoms are available in the alloy melt), and on the other hand also in the overall growth kinetics (as Si atoms have to diffuse through the melt towards the interface from a larger distance). Thus, under similar growth conditions, Si dendrites with smaller tip radii should be observed in the alloy melt as compared to the pure Si melt. In the present work, we describe the morphology of Si dendrites grown at high undercoolings in Al–Si samples. These dendrites nucleate at the surface of levitated droplets and grow along the surface. Thus, after appropriate etching, the shape of the dendrite tips can be evaluated without distortion effects that may blur such results e.g. in metallographic sections.

In the present article, tip shape and radius of Si dendrites grown from pure Si melts as documented in the literature are used for comparison with the Al–Si dendrites. Parabolic dendritic Si tips are compared with the recently developed theory [9–11] on the dendrite tip shapes and the region behind the tip to a distance of several tip radii. The theory is based on analytical results by Ivantsov [12, 13], and represents the generalized shape function smoothly transforms between these limiting cases within the transition region. Good agreement is found for parabolic shapes of Si dendrites grown from pure Si and Al–Si alloys.

2. Experimental procedure

2.1. Electromagnetic levitation

Al-40 wt%Si ingots were prepared by induction melting from pure Al and Si (99.99 mass% of purity) under Ar atmosphere. Cuboid samples of 6–8 mm in width were cut from the bulk ingots for solidification experiments at high undercoolings using the EML method. Prior to solidification in EML, the surface of the sample was ground and cleaned by ethanol to remove the oxide layer and weaken its influence as heterogeneous nucleant. The sample was placed on a sample holder between the two water-cooled copper coils in the EML furnace. The chamber was evacuated to 10^{-6} Pa prior to filling with 6 N helium gas to 3×10^4 Pa. Alternating currents with a frequency of 300 kHz and power up to 5 kW were applied to the levitation coil for generating an alternating electromagnetic field.

According to Lenz's law, the alternate current in the coil creates a repulsive force between coil and sample. When the repulsive force compensates the gravitational force on the sample, it is electromagnetically levitated in the He atmosphere, i.e. there is no contact with any crucible material. With further increasing power, the sample melts due to the induced eddy currents while it remains levitated. After complete melting, the sample adapts a spherical shape. The power of the generator is then further increased, as at higher superheatings the thin oxide on the surface of the sample evaporates/dissolves in the sample. High purity He gas is guided onto the sample to cool it. During the levitation process, the temperature of the sample is measured using a digital infrared pyrometer, and the solidification process, particularly the position of the solidification front, is monitored using a high-speed infrared camera.

2.2. Temperature measurement

According to the Al–Si phase diagram, upon solidification of Al-40 wt%Si, Si will precipitate as primary phase from the melt, until the eutectic reaction, liquid $\rightarrow$ Si + α-(Al), occurs at 577 °C. Since EML is a crucible-free technique, heterogeneous nucleation of Si at the crucible wall is suppressed. The melt droplets cool to high undercoolings, and upon solidification the first recalescence due to nucleation and growth of primary Si occurs. After nucleation of eutectic α-(Al), eutectic solidification occurs on a plateau (see figure 1) near the eutectic temperature. At the end of the eutectic plateau, the sample is fully solid. The real temperature profile during the cooling process of EML was calibrated using the eutectic temperature, $T_{\mathrm{E}}^{\mathrm{ref}} = 577$ °C, following [14]

$$\frac{1}{T} = \frac{1}{T^{\mathrm{pyro}}} + \frac{1}{T_{\mathrm{E}}^{\mathrm{ref}}} + \frac{1}{T_{\mathrm{E}}^{\mathrm{pyro}}}, \tag{1}$$

where T^{pyro} is the measured temperature by the pyrometer, $T_{\mathrm{E}}^{\mathrm{pyro}}$ is the measured eutectic temperature upon cooling, see figure 1(a).

The inset image, figure 1(b), illustrates a snapshot by the high-speed infrared camera of the undercooled melt at the point in time of nucleation of Si. The first recalescence starting at 700 °C is due to the growth of the primary Si phase. The temperature difference between the equilibrium liquidus temperature, 940 °C, and the first recalescence is defined as the growth undercooling ΔT for the primary Si phase. For the case shown in figure 1, the undercooling ΔT is 240 K. After the recalescence, Si phase grows with dendritic structure along the surface of the sample, as shown in figure 1(c). With further decreasing temperature, the growth of Si also proceeds towards the center of the sample. A much smaller recalescence was detected near the eutectic temperature, followed by the plateau lasting for approximately 5 s, which corresponds to the eutectic solidification.

2.3. Microstructure characterization

For characterizing the morphology of the primary Si phase on the surface of the sample solidified in EML, the sample was chemically etched for 5 s using 1 g NaOH + 100 ml H_2O, washed in 5 ml HNO_3 + 100 ml H_2O, once again etched with the same etchant for 5 min and finally washed for a second time. After etching, the surface of the sample was coated with a thin graphite layer by carbon evaporation for microstructure analysis using a scanning electron microscope (SEM, Zeiss Evo 40) equipped with a BSE detector. Let us note that experimental error is about 10%, which corresponds to the average values shown in the graphs below.

The surface of the sample is shown in figure 2, where the bright phase is primary Si, and the remaining area are eutectic. Primary Si with feathery structure (figure 2(a)) and normal dendrites (figure 2(b)) can be seen. A single Si dendrite at a higher magnification exhibiting aligned secondary dendrite arms is shown in figure 2(c). In the same sample, also faceted

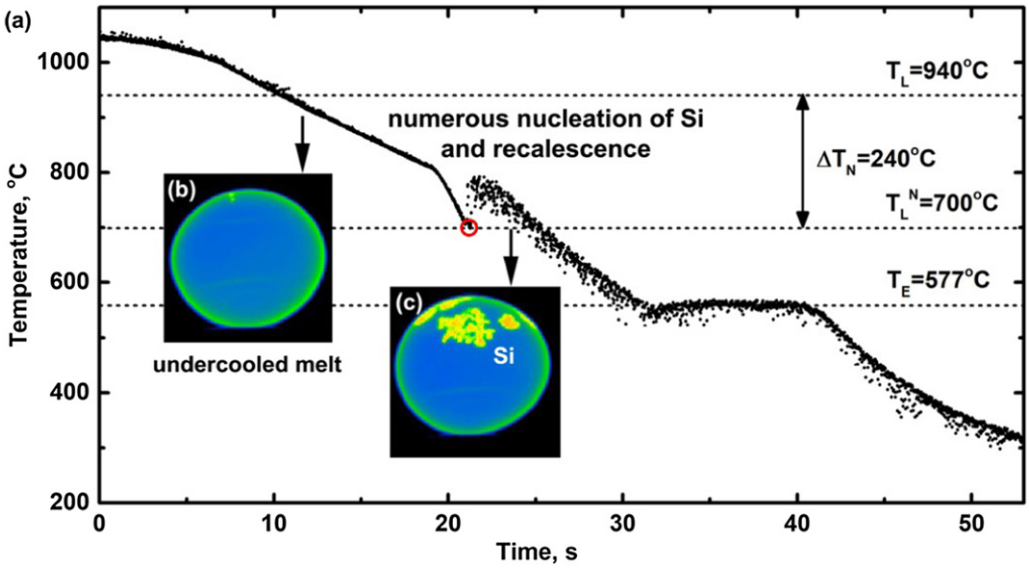

Figure 1. Temperature-time profile during EML of an Al-40Si sample, illustrating the changes in temperature accompanied by different transformations upon solidification (a); high-speed camera images synchronized with the temperature data show that nucleation of Si occurred at an undercooling of 240°C, see inset (b), and the growth of primary Si dendrites (yellow) along the surface, see inset (c).

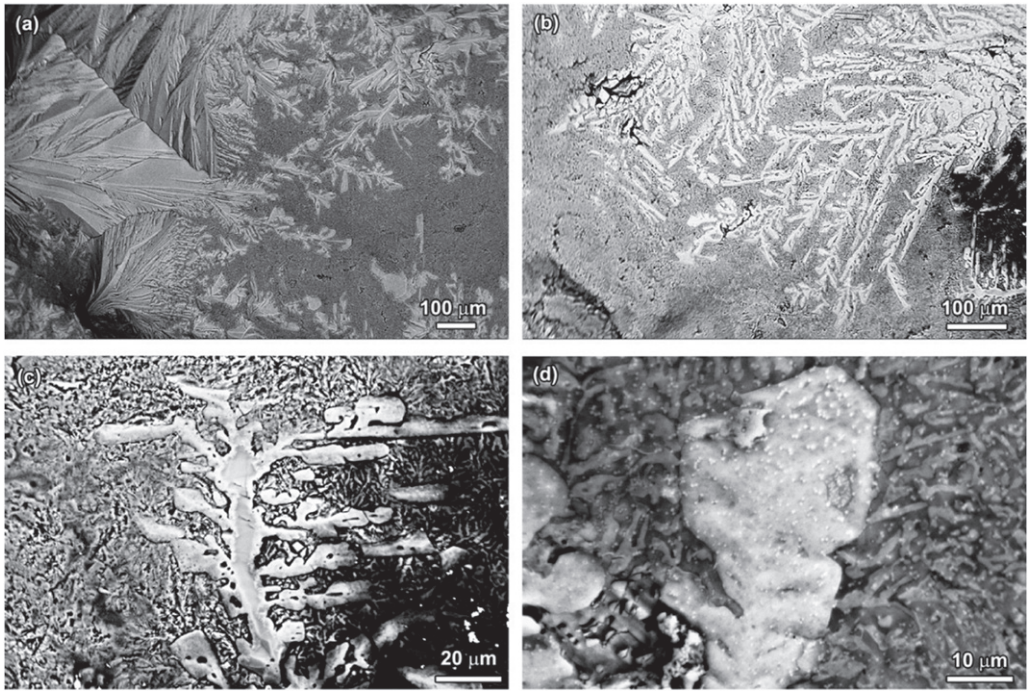

Figure 2. Back-scattered electron (BSE) images of the surface morphology of the Al-40Si sample solidified at an undercooling of 240 K, illustrating the different features of dendritic growth of Si along the surface.

Si dendrites have been observed, as shown in figure 2(d). These results indicate that at the given undercooling of 240 K, growth still occurs in the microstructural transition zone of faceted to non-faceted growth in the Al–Si alloy.

3. Boundary integral method

The boundary integral method [9, 11, 15, 16] allows to describe the steady-state shape of a solid/liquid interface in a binary undercooled melt by a single integro-differential equation in a dimensionless form, where $\zeta(\mathbf{x}, t)$ is the interface function, and $\mathbf{x}$ and t represent the spatial and time variables as

$$-\frac{Q}{m_0 c_p}\left[\Delta - \frac{d_c}{\rho}K - \beta V\left(1 + \frac{\partial\zeta(\mathbf{x},t)}{\partial t}\right) - I_\zeta^T\right] - C_{l\infty} = I_\zeta^C. \tag{2}$$

Here, Q is the latent heat of fusion, m_0 is the liquidus slope, c_p is the specific heat, ρ is the (dimensionless) characteristic

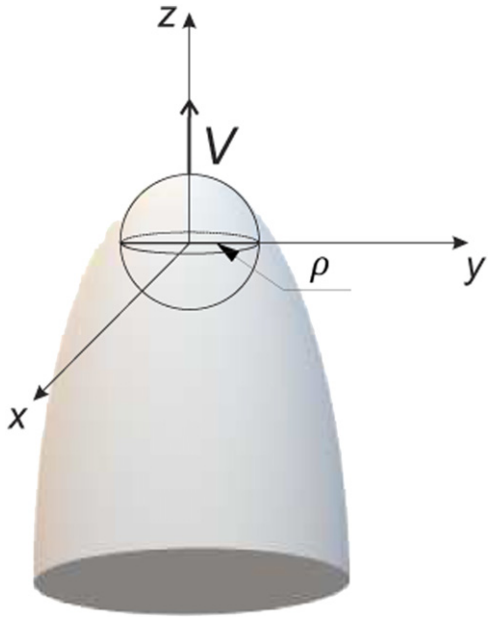

Figure 3. The tip shape of 3D crystal with rotational symmetry given by the shape function (11).

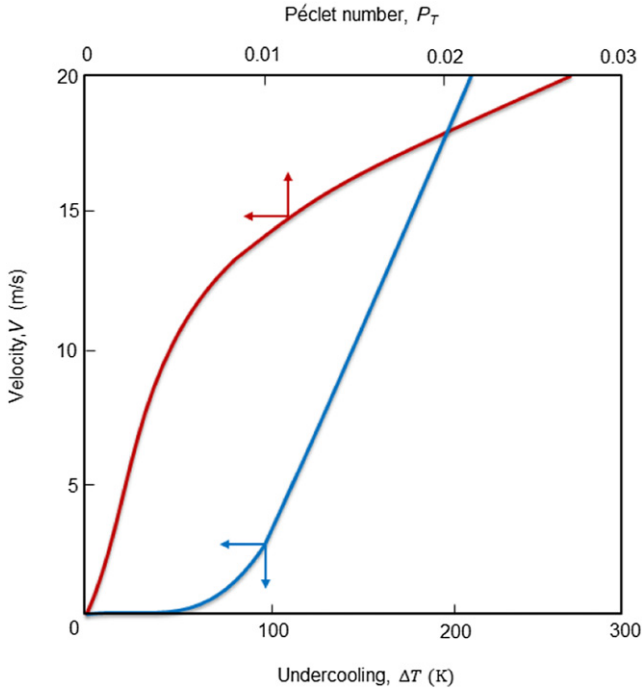

Figure 4. Dendrite tip velocity V and Péclet number P_T as functions of melt undercooling ΔT for the alloy Al-40 wt%Si.

length of the dendrite tip, β is the anisotropic kinetic coefficient, V is the steady-state growth velocity, $C_{l\infty}$ is the solute concentration far from the interface, $\Delta = \left(T_f - T_{l\infty}\right) c_p/Q$ is the undercooling, and K is the interface curvature, which is defined in the three-dimensional (3D) case by

Table 1. Material and calculation parameters for the alloy Al-40 wt%Si.

Parameter	Symbol	Value	Units
Liquidus slope	m	9.53	K/at.%
Hypercooling	T_Q	350	K
Liquidus temperature	T_0	1373	K
Solute diffusion coefficient	D_C	10^{-8}	$m^2\ s^{-1}$
Initial composition	$C_{l\infty}$	40	at.%
Capillary constant	d_0	10^{-9}	m
Thermal diffusivity	D_T	$2.2 \cdot 10^{-5}$	$m^2\ s^{-1}$
Liquid density	ρ_l	$2.7 \cdot 10^3$	$kg\ m^{-3}$
Solute partition coefficient	k_0	0.80	—
Surface energy stiffness	α_d	0.02	—
Solvability constant	σ_0	0.15	—

$$K(\zeta) = -\nabla \cdot \left[\frac{\nabla\zeta}{\sqrt{1+(\nabla\zeta)^2}}\right]. \tag{3}$$

The temperature I_ζ^T and solute concentration I_ζ^C boundary integrals, respectively, are given in the general form for the 3D case [9, 11, 15, 16] as

$$\begin{aligned} I_\zeta^T &= P_T^{3/2}\int_0^\infty \frac{\mathrm{d}\tau}{(2\pi\tau)^{3/2}}\iint_\Omega \left[1+\frac{\partial\zeta(\mathbf{x}_1,t-\tau)}{\partial t}\right] \\ &\quad\times\exp\left[-\frac{P_T}{2\tau}\Sigma(\mathbf{x},\mathbf{x}_1,t,\tau)\right]\mathrm{d}^2x_1, I_\zeta^C \\ &= (1-k_0)P_C^{3/2}\int_0^\infty \frac{\mathrm{d}\tau}{(2\pi\tau)^{3/2}}\iint_\Omega C_i(\mathbf{x}_1,t-\tau) \\ &\quad\times\left[1+\frac{\partial\zeta(\mathbf{x}_1,t-\tau)}{\partial t}\right]\exp\left[-\frac{P_C}{2\tau}\Sigma(\mathbf{x},\mathbf{x}_1,t,\tau)\right] \\ &\quad\times\mathrm{d}^2x_1, \Sigma(\mathbf{x},\mathbf{x}_1,t,\tau) \\ &= |\mathbf{x}-\mathbf{x}_1|^2+[\zeta(\mathbf{x},t)-\zeta(\mathbf{x}_1,t-\tau)+\tau]^2,\ C_i(\mathbf{x},t) \\ &= I_\zeta^C + C_{l\infty}, \end{aligned} \tag{4}$$

where k_0 represents the partition coefficient, $P_T = \rho V/(2D_T)$ and $P_C = \rho V/(2D_C)$ are the thermal and solutal Péclet numbers, respectively, and D_T and D_C are the thermal and solutal diffusivities, respectively. The vector $\mathbf{x}$ has two spatial coordinates x and y in the 3D case, $\mathbf{x} = (x, y)$, and the integration area Ω extends from minus to plus infinity in all its directions.

To define the paraboloidal dendrite shapes (see figure 3), the boundary integrals (4) can be explicitly evaluated, if dendritic growth occurs in steady-state when $\partial\zeta/\partial t$ in (2) and (4) vanishes. To do this, the variable of integration has to be changed as

$$\omega = \frac{(x-x_1)^2}{2\tau}, \qquad z_1 = \frac{y-y_1}{x-x_1} \tag{5}$$

and the temperature and solute concentration boundary integrals can be rewritten for the interface function

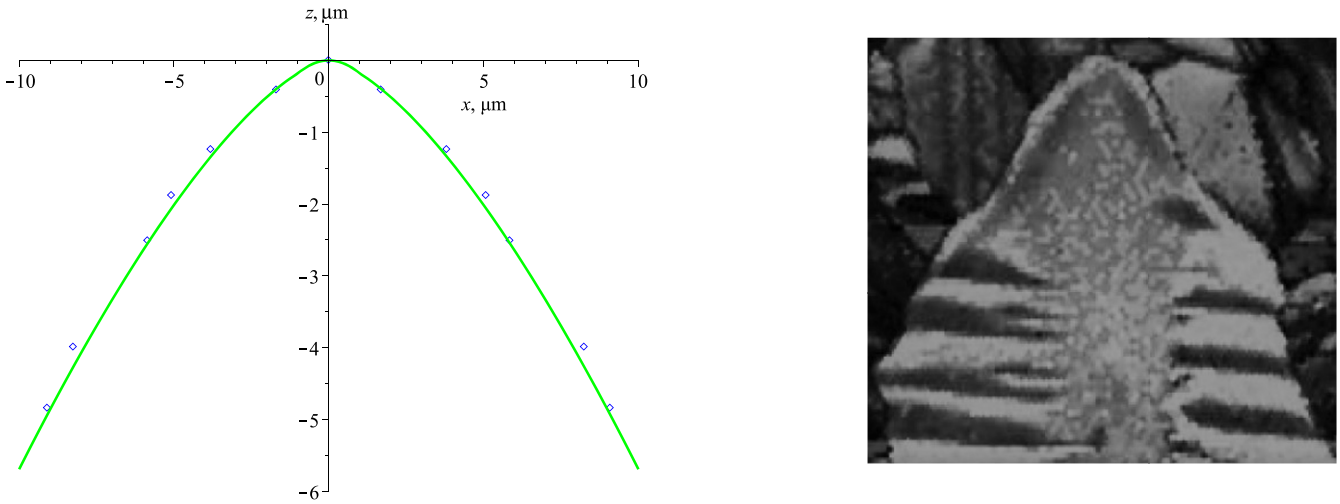

Figure 5. Experimental data [25] of pure Si (dots) in comparison with theoretical predictions (line) for a three-dimensional dendrite (equation (11): $\gamma = 0.18$, $k = 3$).

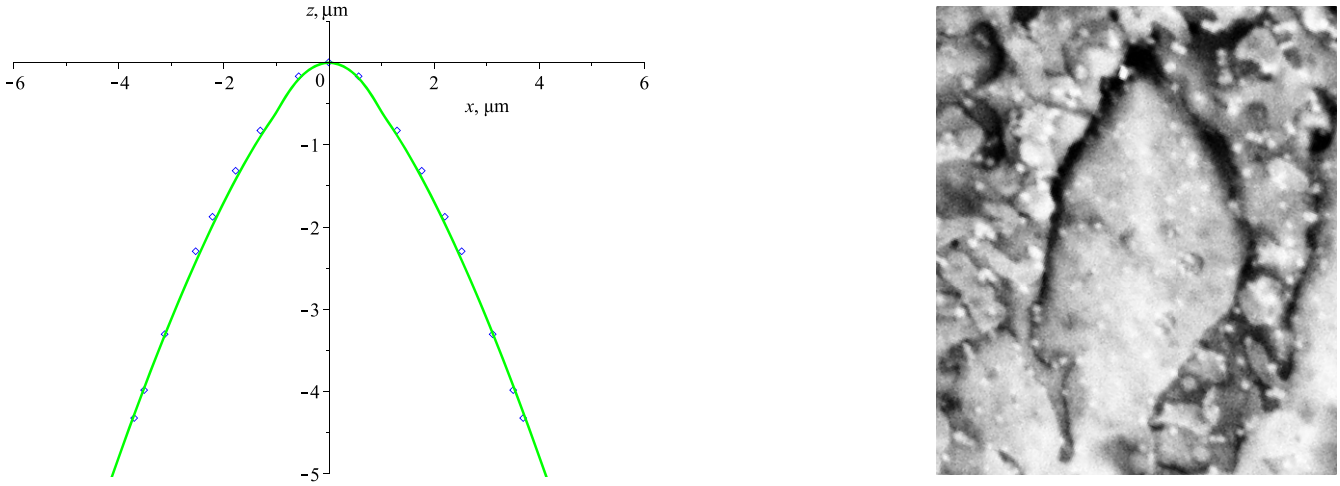

Figure 6. Experimental data of Al–Si (dots) in comparison with theoretical predictions (line) for a three-dimensional dendrite (equation (11): $\gamma = 0.6$, $k = 3$).

$\zeta(x, y) = a\left(x^2 + y^2\right) + b\,(x + y) + c$ $(a < 0)$, where a, b and c represent the constants of the paraboloidal shapes, as

$$I_\zeta^T = -\frac{P_T}{2a}\exp\left(-\frac{P_T}{2a}\right)\int_1^\infty \exp\left(\frac{P_T\eta}{2a}\right)\frac{\mathrm{d}\eta}{\eta},$$

$$I_\zeta^C = \frac{(1-k_0)\,C_{l\infty}\tilde{g}\,(P_C)}{1-(1-k_0)\,\tilde{g}\,(P_C)},$$

$$\tilde{g}\,(P_C) = -\frac{P_C}{2a}\exp\left(-\frac{P_C}{2a}\right)\int_1^\infty \exp\left(\frac{P_C\eta}{2a}\right)\frac{\mathrm{d}\eta}{\eta}. \quad (6)$$

Neglecting the curvature term in equation (2) and using the boundary integral (6), one obtains the expression determining the melt undercooling ahead of the growing dendrite tip in the case of steady-state growth as

$$-\frac{Q}{m_0 c_p}\left[\Delta - \beta V - I_\zeta^T\right] - C_{l\infty} = I_\zeta^C. \quad (7)$$

This expression enables us to find the melt undercooling ΔT as a function of tip velocity V and Péclet number P_T (tip diameter ρ should be substituted from the selection theory [17–24]). Figure 4 shows such dependences for the alloy Al-40 wt%Si (material and calculation parameters are given in the table 1). As is easily seen, these functions monotonously grow with increasing ΔT. According to the theory, non-monotonic growth for Al–Si melts can only occur at high undercooling when the effects of local non-equilibrium of the solidification process take place [17, 19]. This case, however, is not analysed in this paper.

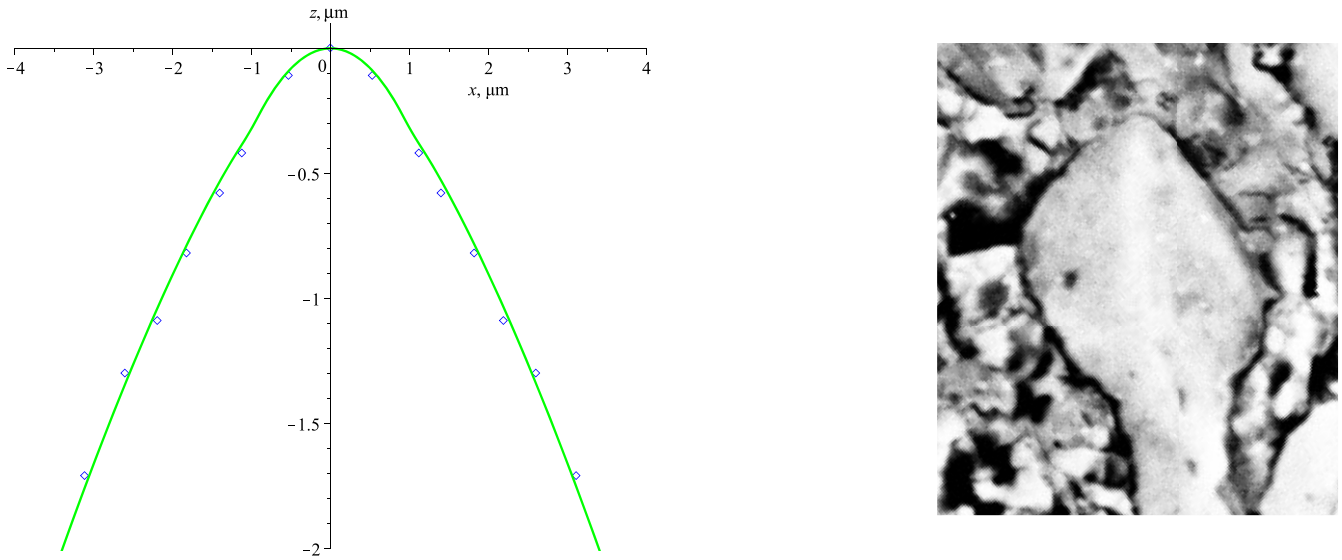

Figure 7. Experimental data of Al–Si (dots) in comparison with theoretical predictions (line) for a three-dimensional dendrite (equation (11): $\gamma = 0.3$, $k = 3$).

4. General dendrite shape functions

The paraboloidal shapes described for the first time by Ivantsov [12, 13] introduce approximate solutions of the boundary integral equation (2) in the vicinity of dendrite tip (at a distance of the order of its tip diameter from the crystal vertex, see figure 1 in [9]). Nevertheless, real dendrites represent complex branching patterns whose shapes differ from ideal shapes described by the Ivantsov solution. The new analytical theory describing dendrite tips at a distance of the order of several tip diameters from the vertex was recently developed in reference [9, 10] for three-dimensional crystals with rotational symmetry. This theory describes the shape of dendritic tips from their vertices to where the secondary branches appear. Following this theory, the tip of the dendrite is at the origin of the coordinate system, its branches point downwards in the direction opposite to the ordinate axis z. The x-axis is at the origin in the direction perpendicular to the z-axis (see figure 3). The shape function for the 3D dendrite tip takes the form [9]

$$z_{\mathrm{AG}}(x) = -\frac{b_S(x)x^2 + b_L(x)|x|^{3/2}}{b_S(x)|x|^{1/2} + b_L(x)|x|^{-1/2}}, \tag{8}$$

where $b_S(x)$ and $b_L(x)$ are arbitrary functions of x that have the following asymptotic behavior

$$\begin{aligned} &\text{at } x \to 0 \qquad b_S(x) \to 0, \qquad b_L(x) \to 1, \\ &\text{at } x \gg 1 \quad b_S(x) \to 1, \qquad b_L(x) \to 0, \end{aligned} \tag{9}$$

and can be written in the form

$$b_S(x) = \exp\left(-\frac{1}{x^{2k}}\right), \qquad b_L(x) = \exp\left(-x^{2k}\right). \tag{10}$$

An important point is that the shape function (8) contains the Ivantsov paraboloidal shape as a limiting case at $x \to 0$, i.e. $z_{\mathrm{AG}}(x) \to -x^2$ at $x \to 0$. In other words, the dendrite tip is paraboloidal only at distances of the order of its tip diameter from the vertex [9]. At larger distances from the vertex, the dendrite shape is described by recently derived shape function (8). Keeping this in mind we can use expression (11) for the melt undercooling ahead of the crystal tip.

5. Shape of Si dendrites in pure Si and Al–Si melts

For comparison with experimental data, let us rewrite the shape function (8) in a form appropriate for the description of dendrite tips in arbitrary spatial axes [9, 10]. For this purpose, we introduce a shape constant γ and rewrite the previously described equation (8) in the form

$$z(x) = \gamma z_{\mathrm{AG}}(x), \tag{11}$$

where $z_{\mathrm{AG}}(x) < 0$ is substituted from expression (8).

In figures 5–7, experimentally gained dendrite shapes grown from pure Si [25] and from an Al–Si melt are compared with the presented 3D theory. Here, we use the shape function (11), where $z_{\mathrm{AG}}(x)$ is substituted from the corresponding law (8) for 3D dendrites. Note that only variables γ (equation (11)) and k (equation (10)) have been altered. It is straightforward to see that the analytical curve follows the experimental observations in excellent agreement in all cases. The dendrite tip radii for the two dendrites grown from the Al–Si melt are 0.25 and 0.5 μm, respectively. This illustrates the scatter in the growth conditions that may vary locally in a levitated droplet at a given undercooling. As expected, the tip radius of the dendrite grown from pure Si melt is coarser, it features a value of 1.0 μm. The growth undercooling in pure Si (80 K) and in the Al–Si alloy (240 K) are substantially different, and so is the growth kinetics that is limited by diffusion in the case of the Al–Si melt, but by atom attachment in the pure Si melt. It is pertinent to note that at a given growth undercooling dendrites from pure Si melt grow faster by one to two orders of

magnitude, than dendrites from Al–Si melt [5]. Due to the fast growth from pure Si the tip radius is refined, which leads to the relatively small difference between the dendrite radii. Nevertheless, as demonstrated by the agreement by the shape functions, in both cases the same scaling law applies.

6. Conclusion

In conclusion, microstructure and morphology of Si crystals grown from pure Si and Al–Si undercooled melts are studied using EML facility. Our experiments show that primary Si can be formed with feathery and ordinary dendritic structures. As this takes place, aligned secondary dendrite arms and faceted Si dendrites can appear at the same undercooling. In addition, the microstructural transition zone with faceted and non-faceted growth takes place. Also, we demonstrate that dendritic crystals growing from pure Si evolve faster by one to two orders of magnitude, than crystals growing from Al–Si melt.

Moreover, the tip shape of silicon dendrites growing from pure Si (literature data [25]), and Al–Si melts (in-house experiments) are compared with recent theory in the temperature range of moderate undercooling. It is problematic to find data on the solidification of Si in this range since it is typical for this substance to set up experiments in either low or high undercooling. Since in-house experiments are new and unpublished before, the comparisons with the theory given in this study constitute scientific novelty.

In this paper, we analyze the tip shapes of Si dendrites grown in pure and binary melts. Despite the different conditions with regard to thermodynamics and kinetics, the shape of dendrite tips of Si features very similar morphologies. Namely, the tip shapes of dendrites satisfy the interface function (11) obtained by sewing together the Ivantsov and Brener asymptotic solutions in [9]. Thus, we confirmed that this interface function well describes the whole region of dendrite tip (its vertex and the region behind it extending up to several dendrite tip diameters) for Si crystals.

Acknowledgments

LVT gratefully acknowledges fruitful discussions about the theoretical results with Prof. Peter Galenko, and financial support from the Russian Science Foundation (Project No. 21-79-10012). MR and DML are grateful for financial support by Deutsche Forschungsgemeinschaft, Grant Re1261/23.

Data availability statement

All data that support the findings of this study are included within the article (and any supplementary files).

ORCID iDs

L V Toropova https://orcid.org/0000-0003-4587-2630
D V Alexandrov https://orcid.org/0000-0002-6628-745X

References

[1] Jackson K A 1984 *Mater. Sci. Eng.* **65** 7
[2] Devaud G and Turnbull D 1985 *Appl. Phys. Lett.* **46** 844
[3] Li D and Herlach D M 1996 *Europhys. Lett.* **34** 423
[4] Ayoma T and Kurybayashi K 2000 *Acta Mater.* **48** 3739
[5] Panofen C and Herlach D M 2007 *Mater. Sci. Eng.* A **449–451** 669–703
[6] Liu R P, Volkmann T and Herlach D M 2001 *Acta Mater.* **49** 439
[7] Lipton J, Kurz W and Trivedi R 1987 *Acta Metall.* **35** 957
[8] Murray J L and McAlister A J 1984 *Bulletin of Alloy Phase Diagrams* **5** 74
[9] Alexandrov D V and Galenko P K 2020 *Phil. Trans. R. Soc.* A **378** 20190243
[10] Alexandrov D V, Toropova L V, Titova E A, Kao A, Demange G, Galenko P K and Rettenmayr M 2021 *Phil. Trans. R. Soc.* A **379** 20200326
[11] Alexandrov D V, Titova E A, Galenko P K, Rettenmayr M and Toropova L V 2021 *J. Phys.: Condens. Matter* **33** 443002
[12] Ivantsov G P 1947 *Dokl. Akad. Nauk SSSR* **58** 567
[13] Ivantsov G P 1952 *Dokl. Akad. Nauk SSSR* **83** 573
[14] Gandin C-A, Mosbah S, Volkmann T and Herlach D M 2008 *Acta Mater.* **56** 3023
[15] Alexandrov D V and Galenko P K 2017 *Physica* A **469** 420
[16] Galenko P K, Alexandrov D V and Titova E A 2018 *Phil. Trans. R. Soc.* A **376** 20170218
[17] Alexandrov D V and Galenko P K 2014 *Phys. - Usp.* **57** 771
[18] Alexandrov D V, Galenko P K and Toropova L V 2018 *Phil. Trans. R. Soc.* A **376** 20170215
[19] Alexandrov D V and Galenko P K 2021 *Phil. Trans. R. Soc.* A **379** 20200325
[20] Langer J S and Hong D C 1986 *Phys. Rev.* A **34** 1462
[21] Barbieri A and Langer J S 1989 *Phys. Rev.* A **39** 5314
[22] Pelcé P and Bensimon D 1987 *Nucl. Phys.* B **2** 259
[23] Kao A, Toropova L V, Krastins I, Demange G, Alexandrov D V and Galenko P K 2020 *JOM* **72** 3123
[24] Kao A, Toropova L V, Alexandrov D V, Demange G and Galenko P K 2020 *J. Phys.: Condens. Matter* **32** 194002
[25] Nagashio K and Kuribayashi K 2005 *Acta Mater.* **53** 3021